

## Research Article

### Numerical Study of a Vortex Ring Interacting with a Three-dimensional Convex Surface

Heng Ren, Genxuan Zhang, Hongshan Guan, Xianfeng Zhang and Wanjun Liu

China Electronics Technology Group Corporation No. 38 Research Institute, Hefei 230031, China

**Abstract:** A vortex ring impinging on a three-dimensional bump is studied using Large Eddy Simulation (LES) for a Reynolds number  $Re = 4 \times 10^4$  based on the initial diameter and translational speed of the vortex ring. The evolution of vortical structures are investigated and an array of flow phenomena are discovered, such as the generation and deformation of secondary vortex ring, formation of loop-like vortices, interaction of vortex rings and the instability and breakdown of vortical structures. The total enstrophy of the flow reasonably elucidates some typical phases of flow evolution. Based on the Fourier analysis of the vertical vorticity, the azimuthal instabilities of the primary vortex ring are studied. Furthermore, the mechanism of vorticity generation on the bump surface has been revealed based on analysis of the boundary vorticity flux.

**Keywords:** Azimuthal instability, large eddy simulation, vortical structure

## INTRODUCTION

As one of the simplest and important forms of vortex motion, vortex rings widely exist in nature and engineering. The interaction of vortex rings with solid or fluid boundaries is a fundamental problem in fluid dynamics and has received considerable attention recent years. The interest in this subject is mainly due to its significant practical applications, such as cavitating rings being used for underwater drilling (Chahine and Genoux, 1983), vortex rings extinguishing gas and oil well fires (Akhmetov *et al.*, 1980) and modeling the interaction between the downburst and the aircraft (Lundgren and Mansour, 1991). However, the underlying flow phenomena and physical mechanisms are still unclear and are worthy of detailed studies.

Vortex rings interacting with a flat wall has been extensively studied. These studies (Walker *et al.*, 1987; Chu *et al.*, 1993; Clercx and Bruneau, 2006; Cheng *et al.*, 2010; Couch and Krueger, 2011) showed that as the primary vortex ring moves gradually toward the wall, its rate of approach slows down and its radius continues to increase. When the Reynolds number of the ring is larger than 500 based on the initial diameter and translational speed of the vortex ring, the formation of the secondary ring occurs and then it interacts with the primary vortex ring. Experimental study (Walker *et al.*, 1987) has revealed that, beyond  $Re = 3000$ , the primary vortex ring will no longer remain stable as it approaches the wall. Thus, the instability of vortex rings should be considered when the Reynolds number becomes large enough.

Comparing with the numerous studies of vortex ring interacting with a flat wall, the investigation relevant to a vortex ring impacting a curved surface is scarce. Orlandi and Verzicco (1993) numerically studied vortex pairs interacting with a two-dimensional circular cylinder with free-slip and no-slip boundary conditions. For the free-slip case, the dipole is observed to split into two vortices and then to rejoin on the cylinder. While for the no-slip interaction, the generation of dipolar and tripolar structures occurs on the cylinder surface. Verzicco *et al.* (1995) further studied this problem. They found that the induced vortices become more apparent as the diameter of the cylinder increases. Allen *et al.* (2007) presented experimental results of a vortex ring impacting a moving sphere. They found that the secondary vorticity generated on the sphere surface results in an acceleration of the sphere and a reduction of the fluid impulse. In a recent investigation, De Sousa (2012) studied a vortex ring impacting a stationary sphere for  $Re = 1000$  using Direct Numerical Simulation (DNS). After the secondary vortex ring is formed, they found its interaction with the primary ring results in the fast decay of circulation for the secondary ring.

In this study, large eddy simulation is utilized to investigate the dynamics and instability of vortical structures when a vortex ring impacts a three dimensional bump at Reynolds number  $Re = 4 \times 10^4$ . To our knowledge, the relevant work has never been performed before. The purpose of this study is to investigate the complex flow phenomena and the underlying mechanisms.

**Corresponding Author:** Heng Ren, China Electronics Technology Group Corporation No. 38 Research Institute, Hefei 230031, China

This work is licensed under a Creative Commons Attribution 4.0 International License (URL: <http://creativecommons.org/licenses/by/4.0/>).

## MATHEMATICAL FORMULATION AND NUMERICAL METHODS

To investigate a vortex ring impinging on a bump, the three dimensional Favre-filtered compressible Navier-Stokes equations in generalized coordinates are used. Large eddy simulation is implemented in the present work for turbulence closure. Some terms in the Favre-filtered equations arising from unresolved scales need to be modelled in terms of resolved scales. Then, dynamic Subgrid-Scale (SGS) models for turbulent flows are employed. A detailed description of the mathematical formulation of the non-dimensionalized equations and the SGS models can be found in the previous work (Xu *et al.*, 2010; Zhang *et al.*, 2014).

The governing equations are numerically solved by a finite volume method. The convective terms are discretized by a second order centered scheme and the viscous terms by a fourth order central scheme. The time advancement is performed using an implicit approximate-factorization method with sub-iterations to ensure the second order accuracy and a fourth order low artificial numerical dissipation is employed to prevent numerical oscillations. Moreover, the present numerical strategy has already been applied successfully to a variety of complex flows and has been verified the reliable calculations.

### Computational overview and validation:

**Computation overview:** According to the schematic as depicted in Fig. 1, a Gaussian vortex ring (Shariff *et al.*, 1994) with radius  $R_0$  is initially placed at  $x_c = (0, 0, H_v)$ , where  $H_v$  represents the distance between the vortex ring center and the bottom wall. The bump has a circular base with a cosine-squared cross section  $z(x, y) = H_b \cos^2(\pi\sqrt{x^2 + y^2}/6)$ , where  $H_b$  is the bump height. The initial translational speed of the vortex ring can be represented as (Saffman, 1978):

$$u_v = \frac{\Gamma}{4\pi R_0} \left( \ln \frac{8R_0}{\sigma_0} - \frac{1}{4} \right), \quad (1)$$

where,  $\sigma_0$  is the initial core radius and  $\Gamma$  is the circulation of the vortex ring. To deal with the instability of the vortex ring, an azimuthal disturbance with an amplitude of  $2 \times 10^4$  is introduced by imposing a radial displacement on the axis of the ring (Shariff *et al.*, 1994; Archer *et al.*, 2008).

In the computation, the slenderness ratio and initial height of the vortex ring are  $\sigma_0/R_0 = 0.2$  and  $H_v/R_0 = 6$ , respectively. The bump height  $H_b/R_0$  is 1.8. The Reynolds number based on the translational speed and the ring diameter is  $Re = 4 \times 10^4$ . The computational domain extends for  $16 R_0$  in the  $x$  and  $y$  directions and  $12 R_0$  in the  $z$  or vertical direction, i.e.,  $L_x/R_0 = L_y/R_0 = 16$ ;  $L_z/R_0 = 12$ . Based on our careful examinations, a mesh of size  $N_x \times N_y \times N_z = 641 \times 641 \times 321$  with a resolution  $R_0 = 40 \Delta x$  is used in the computation. The grid-spacing is uniform in the  $x$  and  $y$

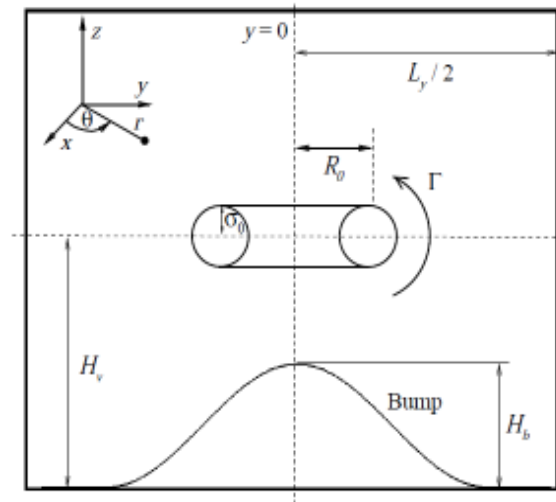


Fig. 1: Schematic diagram of a vortex ring approaching a bump

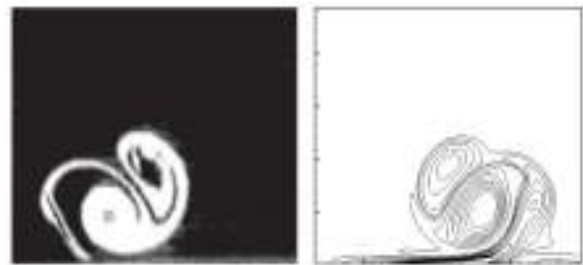


Fig. 2: Vorticity pattern for the interaction between a vortex ring and a flat wall by the experimental observation (Chu *et al.*, 1993) (left panel) and present numerical result (right panel)

directions and a grid stretching in the  $z$  direction is used to increase the grid resolution near the surface. Periodic boundary conditions are employed in the  $x$  and  $y$  directions. No-slip boundary condition is used on the bump surface and a far-field boundary condition is applied in the  $z = L_z$  plane.

**Validation:** Our code is validated through a case about a vortex ring impinging on a flat wall at  $Re = 830$ , which has been investigated by Chu *et al.* (1993) and Cheng *et al.* (2010). The vortex ring is initially placed at the vertical position  $z_0 = 3R_0$  and a grid resolution  $R_0 = 30 \Delta x$  is used for the simulation (Cheng *et al.*, 2010). As shown in Fig. 2, vorticity pattern in the  $y = 0$  plane is compared with the experimental observation of Chu *et al.* (1993). The essential flow features are accurately reproduced in our simulation, including the interaction between the primary and secondary vortex rings and the formation of the tertiary vortex ring. The trajectory of the primary vortex ring center is also compared with the previous results in Fig. 3. It can be

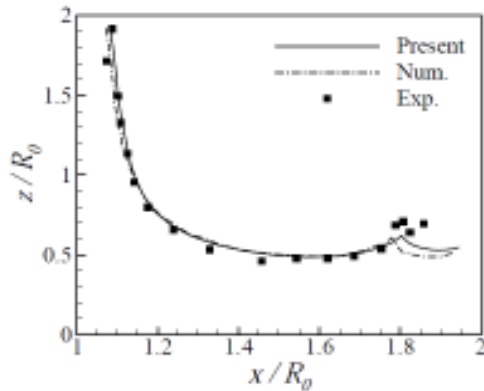


Fig. 3: The trajectory of the primary ring center for  $Re = 830$ . The solid and dashdot lines present the numerical results obtained in this study and by Cheng *et al.* (2010), respectively. The filled symbols represent the experimental data of Chu *et al.* (1993)

seen that our results agree well with the experimental data and numerical results.

### RESULTS AND DISCUSSION

**Vortical structures:** We first investigate the evolution of vortical structures depicted in Fig. 4. From Fig. 4a, when the primary vortex ring moves close to the bump, a vorticity layer is obviously generated on the core surface of bump at  $t = 15.0$ . Then the separation of boundary layer occurs in the adverse pressure gradient region resulting in the generation of secondary vortex

ring at  $t = 17.5$ . Due to the growth of the azimuthal perturbation, the primary vortex ring develops into a wavy-like structure at  $t = 17.5$  and  $20.0$ . Furthermore, by means of Fourier analysis of the azimuthal perturbation, it is identified that the wave number of the most unstable mode for the primary ring is  $k = 11$ , consistent with the theoretical estimate of the dominant mode  $k = 2.26/\sigma_0$  approximately by Maxworthy (1972) and the number of the wavy-like structures observed at  $t = 17.5$  and  $20.0$ . After the primary ring collides with the bump surface, the secondary ring generated lifts up from the surface and then moves over the primary vortex ring. At  $t = 22.5$ , it is seen that the secondary ring has already moved up the primary ring. Subsequently, a variety of loop-like vortices wrapping around both the primary and secondary vortex rings are formed at  $t = 25.0$  and  $27.5$ . The generation of these wrapping vortices is associated with the short-wavelength instability of the vortex rings (Archer *et al.*, 2008). Finally, the complicated interactions of the wrapping vortices and vortex rings over the bump surface result in the breakdown of the vortical structures into small-scale vortices at  $t = 30.0$  and further lead to the vortical flow transition to turbulent state, as shown in Fig. 4h and i.

**Instability of vortical structures:** To quantitatively analyze the development of azimuthal instabilities for the vortex rings, we perform the Fourier decomposition of the vertical vorticity  $\omega_z$  and get  $\bar{A}_k$  (De Sousa, 2012), which denotes the azimuthal perturbation in the

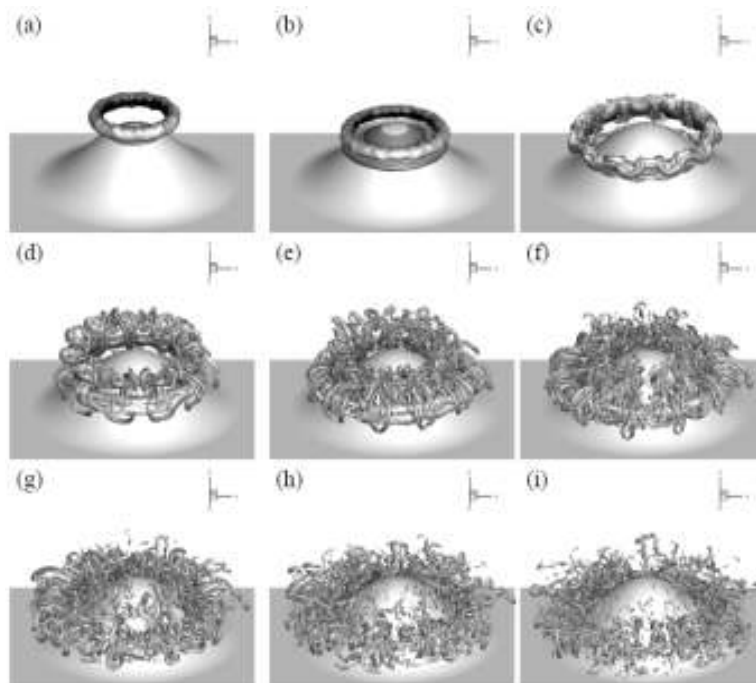


Fig. 4: Evolution of vortical structures depicted by iso-surface of the Q criterion with  $Q = 2$  (a)  $t = 15.0$ , (b)  $17.5$ , (c)  $20.0$ , (d)  $22.5$ , (e)  $25.0$ , (f)  $27.5$ , (g)  $30.0$ , (h)  $32.5$ , (i)  $35.0$

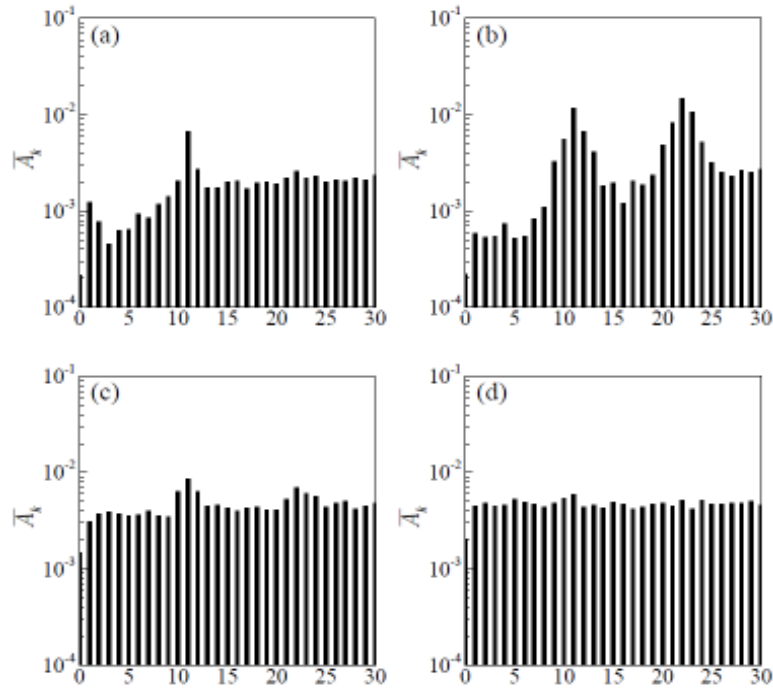


Fig. 5: Azimuthal perturbation of primary vortex ring (a)  $t = 15.0$ , (b)  $20.0$ , (c)  $25.0$ , (d)  $30.0$

vortical structures. The evolution of  $\bar{A}_k$  for the primary vortex ring is plotted in Fig. 5. At  $t = 15.0$ , the vorticity component in the wall-normal direction  $\omega_z$  appears and it is obvious that the dominant mode is  $k = 11$ , consistent with the vortical structures shown in Fig. 4b and c. With the evolution of the vortex ring, the amplitude of  $\omega_z$  increases rapidly implying the fast growth of the instability. At  $t = 20.0$ , the second harmonic  $k = 22$  is apparent and the amplitude of  $\bar{A}_k$  increases considerably, as shown in Fig. 5b. Then with the vertical vorticity  $\omega_z$  breaking into small-scale vorticity, the dominant and second harmonic modes decay rapidly, as depicted in Fig. 5c and d.

**Kinetic energy and enstrophy:** To investigate the global behavior of flow evolution, we further analyze the total kinetic energy and enstrophy in the flow field. Here, the kinetic energy  $E$  and enstrophy  $\Omega$  are defined as:

$$E = \frac{1}{2} \int (\mathbf{u} \cdot \mathbf{u}) dV, \quad (2)$$

$$\Omega = \frac{1}{2} \int (\boldsymbol{\omega} \cdot \boldsymbol{\omega}) dV \quad (3)$$

where,  $\mathbf{u}$  and  $\boldsymbol{\omega}$  represent the resolved quantities obtained by LES and the integral domain is the whole flow field. The total kinetic energy and enstrophy are shown in Fig. 6, where  $E_0$  and  $\Omega_0$  represent the initial kinetic energy and enstrophy, respectively. It can be seen from Fig. 6a that the kinetic energy essentially

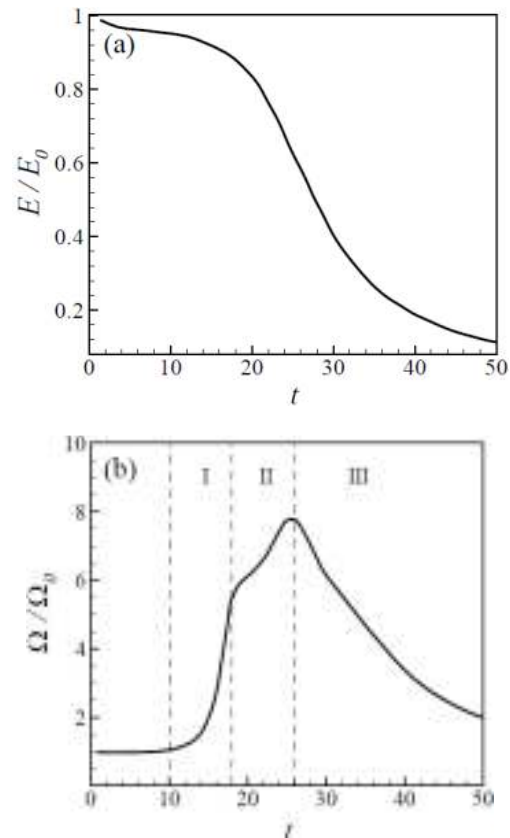


Fig. 6: (a) Total kinetic energy, (b) enstrophy in the flow field. In (b), three phases are described as generation of secondary vortex ring (I), formation of loop-like vortices (II) and breakdown of vortical structures (III)

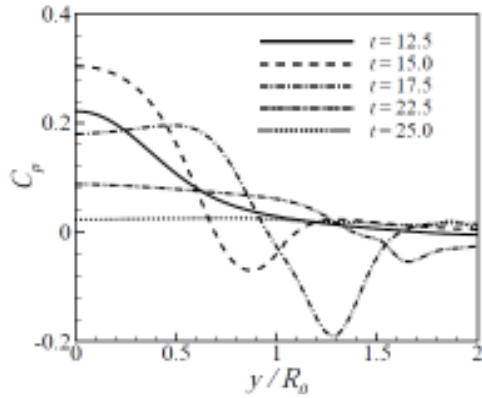


Fig. 7: Pressure coefficient on the bump surface along  $x = 0$

decreases with the flow evolution due to viscous dissipation. With evolution of the vortices, the kinetic energy reduces smoothly during the boundary-layer separation and secondary-vortex generation and decreases quickly as the vortices break down into small-scale ones.

Figure 6b shows the time-dependent enstrophy, which is closely associated with the evolution of vortices. Before  $t = 10.0$  approximately, the vortex ring is somewhat far from the bump and the enstrophy is almost constant. During  $10.0 < t < 18.0$ , the enstrophy grows considerably due to the generation of the secondary vortex as typically depicted in Fig. 4a and b. Then, because of the generation of the loop-like vortices as well as the stretching and deformation of the primary and secondary vortices, the enstrophy

continuously increases and reaches its maximum at approximately  $t = 26.0$ . Then, as the vortices break into small-scale ones, the enstrophy decreases quickly.

**Pressure and boundary vorticity flux on the surface:**

The pressure coefficient is defined by  $C_p = R_0^2(p - p_\infty) / (\rho U_0^2)$ , where  $p_\infty$  represents the far field pressure. Figure 7 shows the distributions of pressure coefficient along  $x = 0$ . As the vortex ring is approaching the bump, the pressure distribution on the bump core region increases gradually such as from  $t = 12.5$  to  $15.0$ . It is seen that the negative pressure coefficient on the vortex ring impacting region occurs at  $t = 15.0$ . Then, as the secondary vortex ring is generated at  $t = 17.5$  as shown in Fig. 4b, the negative pressure coefficient becomes more obvious and the pressure distribution over the bump core region reduces gradually. Subsequently, after the vortex ring collides with the bump, the pressure distribution varies smoothly, such as at  $t = 22.5$  and  $25.0$  in Fig. 7.

To clearly demonstrate the pressure distribution on the bump, Fig. 8 shows the pressure contours on the surface. It is seen that the contours of the pressure coefficient are smooth distribution in the azimuthal direction at  $t = 12.5$  and  $15.0$ . Moreover, the region with negative distribution at  $t = 15.0$  is related to the vortex ring impacting on the bump surface. Then, the contours become the wave-like azimuthal distribution at  $t = 17.5$ , which is reasonably related to the wavy-like structure of the primary vortex ring caused by the azimuthal instability as exhibited in Fig. 4b.

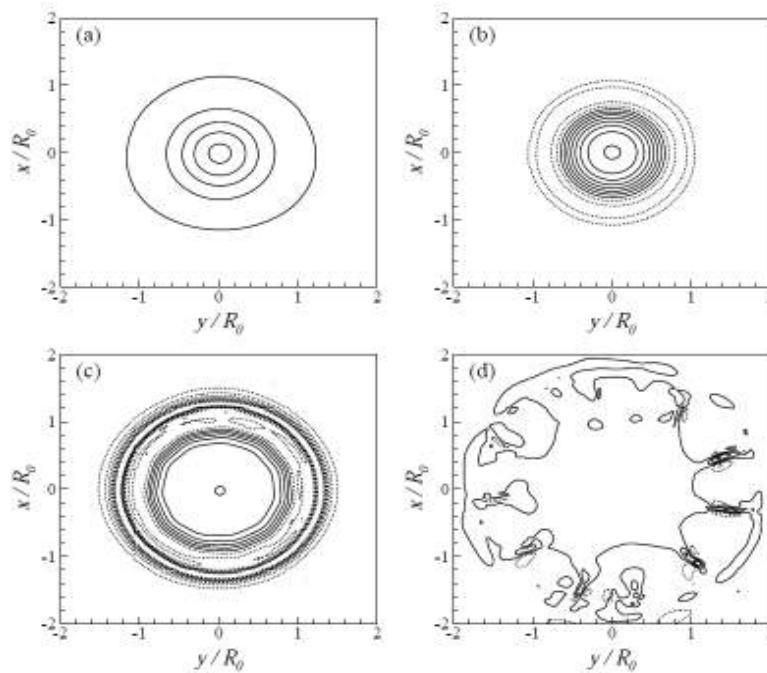


Fig. 8: Contours of the pressure coefficient on the bump surface (a)  $t = 12.5$ , (b)  $15.0$ , (c)  $17.5$ , (d)  $22.5$ . Here, solid and dashed lines denote positive and negative values, respectively; the contour increment is  $\Delta C_p = 0.04$  with  $|C_p| \leq 0.3$

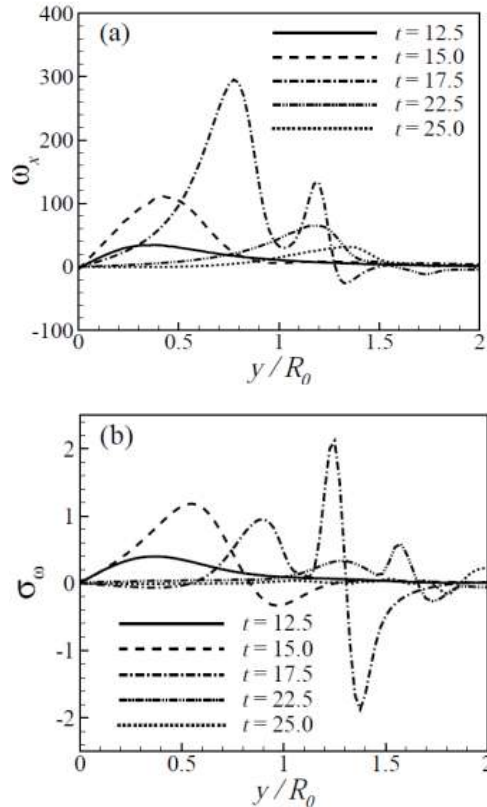


Fig. 9: (a) Vorticity  $\omega_x$  and (b) BVF  $\sigma_\omega$  on the surface along  $x = 0$

Furthermore, the contours of the pressure coefficient at  $t = 22.5$  present some local patterns along the azimuthal direction, corresponding to the loop-like vortices wrapping around both the primary and secondary vortex rings.

Further, for the present flow with a high Reynolds number, the Boundary Vorticity Flux (BVF) can be approximately written as (Xu *et al.*, 2010):

$$\sigma_\omega = \nu \partial \omega / \partial n = \mathbf{n} \times \nabla p / \rho \quad (4)$$

where,  $\nu$  is the kinematic viscosity and  $n$  is the normal unit vector on a solid wall. This relation is reasonably examined based on the present calculated data. Thus, we can learn that the BVF is in turn dominated by the tangent pressure gradient on the surface, which also becomes a cause of new vorticity (Xu *et al.*, 2010). To analyze the vorticity and the BVF, Fig. 9 shows the distributions of vorticity component  $\omega_x$  and BVF  $\sigma_\omega$  on the bump surface. It can be seen that both the magnitudes of  $\omega_x$  and  $\sigma_\omega$  increase rapidly as the primary vortex ring moves close to the bump. At  $t = 17.5$ , the magnitudes reach a relatively high value. Subsequently, the magnitudes decrease gradually, indicating that the generation of vorticity from the bump surface becomes weak.

## CONCLUSION

The interaction between a vortex ring and a three-dimensional bump has been studied by means of the large eddy simulation technique. The vortical flow phenomena and the underlying physical mechanisms were investigated and are summarized briefly as follows. As a vortex ring impinges on a bump, an array of vortical flow phenomena occur, such as the generation and deformation of secondary vortex ring, the formation of loop-like vortices, the interaction of vortex rings and the instability and breakdown of vortical structures. The total kinetic energy and enstrophy have been investigated to reveal the different stages of flow evolution. Based on the Fourier analysis of the vertical vorticity, the azimuthal instabilities of the primary vortex ring were studied. It is found that the dominant mode of the azimuthal instability is  $k = 11$ , consistent with the theoretical estimate  $k = 2.26/\sigma_0$ . Moreover, the vorticity generation on the bump surface has been analyzed and it is noticed that the generation of secondary vortex ring reasonably corresponds to large BVF and subsequently the vorticity generation from the bump surface becomes weak based on the variation of BVF.

## REFERENCES

- Akhmetov, D.G., B.A. Lugovtsov and V.F. Tarasov, 1980. Extinguishing gas and oil well fires by means of vortex rings. *Combust. Explo. Shock+*, 16: 490-494.
- Allen, J.J., Y. Jouanne and B.N. Shashikanth, 2007. Vortex interaction with a moving sphere. *J. Fluid Mech.*, 587: 337-346.
- Archer, P.J., T.G. Thomas and G.N. Coleman, 2008. Direct numerical simulation of vortex ring evolution from the laminar to the early turbulent regime. *J. Fluid Mech.*, 598: 201-226.
- Chahine, G.L. and P.F. Genoux, 1983. Collapse of a cavitating vortex ring. *J. Fluid Eng.*, 105: 400-405.
- Cheng, M., J. Lou and L.S. Luo, 2010. Numerical study of a vortex ring impacting a flat wall. *J. Fluid Mech.*, 660: 430-455.
- Chu, C.C., C.T. Wang and C.S. Hsieh, 1993. An experimental investigation of vortex motions near surfaces. *Phys. Fluids A-Fluid*, 5: 662-676.
- Clercx, H.J.H. and C.H. Bruneau, 2006. The normal and oblique collision of a dipole with a no-slip boundary. *Comput. Fluids*, 35: 245-279.
- Couch, L.D. and P.S. Krueger, 2011. Experimental investigation of vortex rings impinging on inclined surfaces. *Exp. Fluids*, 51: 1123-1138.
- De Sousa, P.J.S.A.F., 2012. Three-dimensional instability on the interaction between a vortex and a stationary sphere. *Theor. Comp. Fluid Dyn.*, 26: 391-399.

- Lundgren, T.S. and N.N. Mansour, 1991. Vortex ring bubbles. *J. Fluid Mech.*, 224: 177-196.
- Maxworthy, T., 1972. The structure and stability of vortex rings. *J. Fluid Mech.*, 51: 15-32.
- Orlandi, P. and R. Verzicco, 1993. Vortex rings impinging on walls: Axisymmetric and three dimensional simulations. *J. Fluid Mech.*, 256: 615-646.
- Saffman, P.G., 1978. The number of waves on unstable vortex rings. *J. Fluid Mech.*, 84: 625-639.
- Shariff, K., R. Verzicco and P. Orlandi, 1994. A numerical study of three-dimensional vortex ring instabilities: Viscous corrections and early nonlinear stage. *J. Fluid Mech.*, 279: 351-375.
- Verzicco, R., J.B. Flor, G.J.F. Van Heijst and P. Orlandi, 1995. Numerical and experimental study of the interaction between a vortex dipole and a circular cylinder. *Exp. Fluids*, 18: 153-163.
- Walker, J.D.A., C.R. Smith, A.W. Cerra and T.L. Doligaski, 1987. The impact of a vortex ring on a wall. *J. Fluid Mech.*, 181: 99-140.
- Xu, C.Y., L. W. Chen and X.Y. Lu, 2010. Large eddy simulation of the compressible flow past a wavy cylinder. *J. Fluid Mech.*, 665: 238-273.
- Zhang, J.P., M.Y. Xu and J.C. Mi, 2014. Large eddy simulations of a circular orifice jet with and without a cross-sectional exit plate. *Chinese Phys. B*, 23: 044704.